A quantum-classical eigensolver using multiscale entanglement renormalization

Qiang Miao and Thomas Barthel
Department of Physics, Duke University, Durham, North Carolina 27708, USA
(Dated: July 20, 2021)

We propose a variational quantum eigensolver (VQE) for the simulation of strongly-correlated quantum matter based on a multi-scale entanglement renormalization ansatz (MERA) and gradient-based optimization. This MERA quantum eigensolver has substantially lower computation costs than corresponding classical algorithms. Due to its narrow causal cone, the algorithm can be implemented on noisy intermediate-scale (NISQ) devices and still describe very large systems. It is particularly attractive for ion-trap devices with ion-shuttling capabilities. While the total number of required qubits grows logarithmically in the size of the simulated system, the number of qubits needed in the interaction region is system-size independent. Translation invariance of the simulated systems can be used to make computation costs square-logarithmic in the system size and describe the thermodynamic limit. We demonstrate the approach numerically for a MERA with Trotterized disentanglers and isometries. With a few Trotter steps, one recovers the accuracy of the full MERA.

I. INTRODUCTION

The complexity of quantum many-body systems makes it a formidable challenge to understand the properties of quantum matter, in particular in strongly correlated regimes where perturbative approaches fail. Hence, powerful classical simulation techniques like quantum Monte Carlo [1–4] and tensor networks states (TNS) [5–11] have been developed. A strength of TNS techniques is that they are also applicable for frustrated quantum magnets and fermionic systems [12–16], where quantum Monte Carlo is hampered by the negative-sign problem [17, 18]. These classes of systems include candidate spin liquid materials [19–23], fractional quantum Hall physics [24, 25], and high-temperature superconductors [26, 27].

Let us consider a lattice system with N sites, each associated with a site Hilbert space of dimension d such that the total Hilbert space has dimension d^N . The idea of TNS is to approximate the many-body state by a network of partially contracted tensors. The tensors may carry physical indices that label site basis states and additional bond indices of dimension χ which are contracted with corresponding indices of other tensors. The structure of the network and the required bond dimension χ are adapted to the entanglement structure in the system. Typically, the more entangled a system is, the larger χ needs to be in order to achieve the desired approximation accuracy. To approximate the ground state of a given model H by a TNS $|\Psi\rangle$, one minimizes the energy $\langle \Psi | \hat{H} | \Psi \rangle$ with respect to the tensor elements. The beauty of the approach is that computation costs for optimization steps are reduced from exponential in N to polynomial in N. In particular, they are linear in N for matrix product states (MPS) [5, 6, 10, 28, 29], projected entangled pair states (PEPS) [7, 8, 30–32] and the multi-scale entanglement renormalization ansatz (MERA) [9, 33]. For homogeneous MERA, one can reduce the cost to $\mathcal{O}(\log N)$ and even access the thermodynamic limit $N \to \infty$. However, the classical computation time may scale with a high power of the bond dimension χ . While they are only $\mathcal{O}(\chi^3)$ for MPS in

one-dimensional (1D) systems [6, 29], they are $\mathcal{O}(\chi^{7...9})$ for 1D MERA [34], $\mathcal{O}(\chi^{10...12})$ for 2D PEPS [35, 36], and $\mathcal{O}(\chi^{16...28})$ for 2D MERA [37, 38]. Hence, practicable χ are usually rather small, which limits the approximation accuracy.

In this work, we propose and analyze a hybrid quantum-classical variational eigensolver [39] to overcome these limitations, where many-body ground states are approximated by adapted MERA states and (small) quantum computers are employed to efficiently execute tensor contractions. In this context, MERA have four advantages over other TNS: (i) MERA can be applied for systems with any number of spatial dimensions, (ii) all tensors are unitary or isometric, which allows for a rather direct implementation on quantum computers, (iii) sets of MERA are closed which implies that optimizers always exist [40], and (iv) MERA expectation values for local operators depend only on narrow causal cones such that they can be evaluated exactly and large systems can be simulated on noisy intermediate-scale (NISQ) devices. Quantum algorithms using MPS for 1D systems were recently suggested in Refs. [41–44]. Two prominent quantum-computing platforms are superconducting qubits [45, 46] and ions in electromagnetic traps [47, 48]. Ion-trap systems with qubit shuttling capabilities [49– 51 are particularly interesting for the quantum MERA scheme. In total, one needs $\mathcal{O}(\log N)$ qubits. But, in each preparation (time) step, only a system-size independent number of qubits needs to be acted upon with quantum gates, corresponding to the width of the causal cone. After each step, some qubits can be shuttled out of the interaction region (quantum register), and new ones can be moved in.

II. MERA ADAPTED FOR QUANTUM COMPUTERS

A MERA [9, 33] is a hierarchical TNS motivated by the real-space renormalization group [52–54]: In each renormalization step $\tau = 1, \ldots, T$, unitaries with small spatial

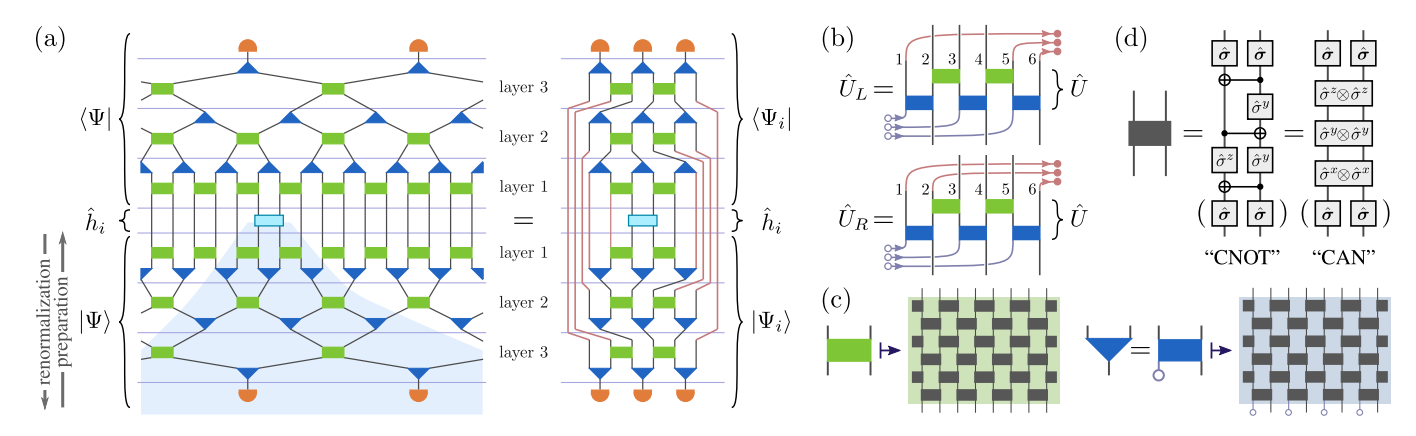


FIG. 1. **TMERA structure and implementation.** (a) Expectation value $\langle \Psi | \hat{h}_i | \Psi \rangle$ for a homogeneous binary 1D MERA $|\Psi\rangle$ with T=3 layers. The MERA consists of disentanglers (boxes) and isometries (triangles). Contraction lines between the tensors correspond to renormalized site vector spaces with dimension χ . The shaded region indicates the causal cone for a two-site operator \hat{h}_i . It has width three, i.e., contains at most three renormalized sites in each layer. Only causal-cone states like $|\Psi_i\rangle$, associated to \hat{h}_i , need to be generated on the quantum computer. (b) Isometries can be realized as unitaries where some input qubits are initialized in a reference state like $|0\rangle$ (open circles). In ion-trap systems, such $|0\rangle$ qubits can be shuttled in and others (filled circles) can be shuttled out of the quantum register when applying the layer-transition maps. Only those inside the causal cone remain. (c) A Trotter structure with t steps is imposed on each MERA tensor, making it a circuit of two-qubit gates. Here, t=3 and $\chi=16$, i.e., q=4 qubits per contraction line. (d) Each Trotter gate can be implemented using CNOTs and single-qubit rotations or, equivalently, single and two-qubit rotations. The specified Pauli operators generate the corresponding rotations (1), and $\hat{\sigma}$ refers to a general single-qubit rotation.

support are applied to disentangle the system to some extent, before isometries are applied in order to map a block of b sites into a new renormalized site. In the process, states that are not important for the representation of the ground state are discarded. With a branching ratio of b, this process ends in a single renormalized site after $T \sim \log_b N$ steps, and the resulting single-site problem can be solved exactly. While the physical site Hilbert spaces have dimension d, Hilbert spaces of renormalized sites have dimension χ . Seen in reverse, the renormalization group scheme defines a many-body state $|\Psi\rangle$. This state is a MERA with bond dimension χ . It consists of T layers, each comprising the unitary disentanglers and isometries of a renormalization step. Optimizing the tensor elements to minimize the energy expectation value $E = \langle \Psi | \hat{H} | \Psi \rangle$, one obtains a groundstate approximation.

In principle, it is straightforward to prepare a MERA $|\Psi\rangle$ on quantum computers. Assume $\chi=2^q$ such that every renormalized site corresponds to q qubits. A disentangler that acts on n (renormalized) sites is a $\chi^n\times\chi^n$ unitary acting on nq qubits. It can be decomposed into a circuit of $\mathcal{O}(4^{nq})$ single-qubit and CNOT gates [55–57]. An isometry that maps n sites into m>n can be implemented as a unitary acting on nq qubits and (m-n)q additional ones initialized in state $|0\rangle$. It requires $\mathcal{O}(2^{(n+m)q})$ single-qubit and CNOT gates [58].

For simplicity, we assume a Hamiltonian $\hat{H} = \sum \hat{h}_i$ with finite-range interaction terms \hat{h}_i . As exemplified in Fig. 1a, a lot of tensors cancel in expectation values $\langle \Psi | \hat{h}_i | \Psi \rangle$ due to their isometric property. The causal cone of \hat{h}_i comprises all tensors that can influence the expectation value, and we define $|\Psi_i\rangle$ as the corresponding

causal-cone TNS such that $\langle \Psi | \hat{h}_i | \Psi \rangle = \langle \Psi_i | \hat{h}_i | \Psi_i \rangle$. For a binary 1D MERA, disentanglers act on n=2 sites and the cost to evaluate $\langle \Psi_i | \hat{h}_i | \Psi_i \rangle$ would scale in q as $\mathcal{O}(4^{2q})$. Hence, the cost for the evaluation of an energy gradient would scale as $\mathcal{O}(4^{4q} = \chi^8)$. This is only a modest improvement over the scaling $\mathcal{O}(\chi^9)$ of the classical computation cost. This turns out to be true for various MERA structures as discussed in Appx. A. Hence, we need to impose further structure on the MERA to reduce the computational complexity.

III. TROTTERIZED TENSORS

There are many options for this. Here, we choose to impose a Trotter structure on the MERA tensors. In particular, they shall consist of t Trotter steps, each comprising local unitary gates that act on, say, two nearest neighbor qubits; see Fig. 1c. For tensors that act on n (renormalized) sites, each Trotter step consists of $\mathcal{O}(nq)$ local gates. For a Trotterized MERA (TMERA) with T layers, the evaluation of a local expectation value $\langle \Psi_i | \hat{h}_i | \Psi_i \rangle$ then requires $\mathcal{O}(Tt)$ time on the quantum computer. Exploiting translation invariance as discussed below, the quantum computation of the energy gradient requires $\mathcal{O}(T^2t^2nq)$ time. Our simulations suggest that the energy error of the TMERA decreases according to a power law until getting close to the accuracy of the MERA with full tensors (fMERA). A slower (logarithmic) decay follows, which one should avoid and rather increase $\chi = 2^q$. The optimal t seems to follow a power law $t \propto q^{\alpha}$ with a modelspecific exponent $\alpha > 1/D$, where D denotes the number of spatial dimensions. In this sense, the quantum costs $\mathcal{O}(T^2t^2q) = \mathcal{O}(T^2(\log_2\chi)^{2\alpha+1})$ are poly-logarithmic in the bond dimension χ , while the time complexity of the classical algorithms scales with a high power in χ , specifically, $\mathcal{O}(T\chi^{7...9})$ for D=1 and $\mathcal{O}(T\chi^{16...28})$ for D=2.

IV. HYBRID OPTIMIZATION ALGORITHM

In classical computations, MERA states are optimized by evaluating the so-called environment for each tensor and updating tensors one by one [59]. On a quantum computer, we can only measure observables, and the tensor environment is not accessible. The hybrid algorithm works as follows. The Trotter gates can be written as small circuits, parametrized through the angles $\theta = (\theta_1, \theta_2...)$ of rotations

$$\hat{R}_{\hat{\sigma}}(\theta) := e^{-i\theta\hat{\sigma}/2} = \mathbb{1}\cos\frac{\theta}{2} - i\hat{\sigma}\sin\frac{\theta}{2}$$
 (1)

with respect to Hermitian unitary operators $\hat{\sigma}$ like the Pauli matrices $\{1, \hat{\sigma}^x, \hat{\sigma}^y, \hat{\sigma}^z\}$ or tensor products thereof. A standard choice is depicted in Fig. 1d. It comprises three CNOT gates, one $\hat{\sigma}^z$ and two $\hat{\sigma}^y$ single-qubit rotations, as well as four general single-qubit gates [60, 61]. The number of angles per Trotter gate agrees with dim SU(4) = 15 and reduces to nine angles when exploiting the unitary gauge freedoms in the TMERA. The energy gradient $\partial_{\theta} E$ can be evaluated by measuring

$$\partial_{\theta_j} E = \frac{1}{2} \left[E(\theta_j + \pi/2) - E(\theta_j - \pi/2) \right], \qquad (2)$$

where all angles except for θ_j are kept fixed. A derivation is given in Appx. C. The energy can now be minimized by a gradient-based algorithm like L-BFGS [62, 63].

In experiments, two-qubit gates are typically much more costly than single-qubit gates. For ion-trap and superconducting systems, typical single-qubit gate times are $\sim 10 \ \mu s$ and $\sim 30 \ ns$, respectively, where two-qubit gates require $\sim 100 \ \mu s$ and $\sim 200 \ ns$, respectively [64– 67]. The CNOT parametrization (Fig. 1d) of the Trotter gates has the drawback that CNOT gates require twoqubit rotations with large angles. In the ion-trap and superconducting systems, CNOT is implemented using an effective Ising $\hat{\sigma}^{\alpha} \otimes \hat{\sigma}^{\alpha}$ interaction with rotation angle $\theta = \pi/2$ [67–70]. A better choice is then the canonical (CAN) parametrization in Fig. 1d that comprises three native $\hat{\sigma}^{\alpha} \otimes \hat{\sigma}^{\alpha}$ rotations $(\alpha = x, y, z)$ and four general single-qubit rotations [71, 72]. Benchmark simulations below show that the occurring two-qubit angles for this parametrization are rather small. Furthermore, we find that the optimization works best in a parametrizationfree fashion. Such a Riemannian quasi-Newton method is described in Appx. C.2.

V. TRANSLATION INVARIANCE

For translation-invariant systems, the interaction terms \hat{h}_i are translates of the same operator \hat{h} . Correspondingly, we can reduce the number of variational parameters. A homogeneous MERA has translation-invariant layers, i.e., the tensors of all b-site cells in layer τ agree. A binary 1D MERA, for example, is then characterized by a single disentangler and a single isometry for each layer. For a heterogeneous system, the derivatives (2) can be evaluated by measuring expectation values for all terms h_i that have the tensor of angle θ_j in their causal cone. In total, this requires $\mathcal{O}(TN=N\log_b N)$ measurements. With translation invariance, this can be reduced to $\mathcal{O}(T)$ by introducing auxiliary qubits:

For the 1D case illustrated in Fig. 1, there are two unitary maps \hat{U}_L and \hat{U}_R and either of them has to be applied to progress in the preparation of the causal-cone state $|\Psi_i\rangle$ from layer τ to $\tau-1$. The specific sequence depends on the location i of the interaction term. In order to evaluate the energy density $e:=\frac{1}{N}\langle\Psi|\hat{H}|\Psi\rangle=\frac{1}{N}\sum_i\langle\Psi_i|\hat{h}_i|\Psi_i\rangle$ for the entire system at once, we can replace $\hat{U}_{L,R}$ by their convex combination such that we obtain the state on layer $\tau-1$ as

$$\hat{\rho}^{(\tau-1)} = \frac{1}{2} \left(\hat{U}_L \hat{\rho}^{(\tau)} \hat{U}_L^{\dagger} + \hat{U}_R \hat{\rho}^{(\tau)} \hat{U}_R^{\dagger} \right). \tag{3}$$

For the experimental implementation, such quantum channels can be lifted to unitary evolution on a larger Hilbert space [73, 74]. For Eq. (3), adding a single auxiliary qubit per layer is sufficient such that $e=\langle\Psi^{(0)}|\hat{h}\otimes\mathbb{1}|\Psi^{(0)}\rangle$ with

$$|\Psi^{(\tau-1)}\rangle = \frac{1}{\sqrt{2}} \left(\hat{U}_L |\Psi^{(\tau)}\rangle \otimes |0\rangle_{\text{aux}} + \hat{U}_R |\Psi^{(\tau)}\rangle \otimes |1\rangle_{\text{aux}} \right). \tag{4}$$

In this case, \hat{U}_L and \hat{U}_R are simply related by the site permutation (2345) \mapsto (5234) on the output of \hat{U} in Fig. 1b. Hence, transformation (4) can be realized by initializing the auxiliary qubit in the state $(|0\rangle + |1\rangle)/\sqrt{2}$, applying \hat{U} , and then a controlled site permutation, conditioned on the auxiliary qubit.

Finally, for a homogeneous MERA, let $L_x, L_y \dots$ denote the linear sizes of the system, chosen such that the causal cone of no local interaction term closes upon itself along any of the spatial dimensions. Repeating the MERA in any spatial direction $(L_\alpha \mapsto nL_\alpha)$ defines families of MERA, which all have the same energy density e. In particular, the results capture the thermodynamic limit $N \to \infty$.

VI. ION SHUTTLING

An attractive feature of the proposed quantumclassical TMERA algorithm is that, while we can simulate large systems, at any stage, only a small number

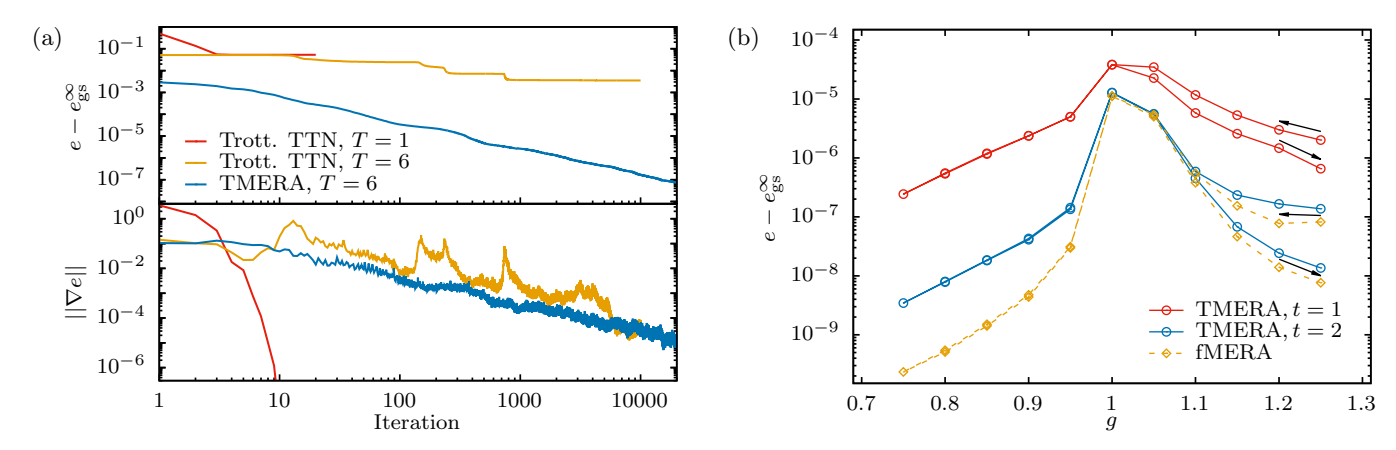


FIG. 2. Benchmark simulations. The plots show the convergence and accuracy of energy densities e for the transverse Ising model (5) using homogeneous modified binary MERA with T=6 layers and bond dimension $\chi=8$ (q=3). Panel (a) shows the convergence at g=1.25 for TMERA with t=2, starting from the product state with state $e^{-i\frac{\pi}{8}\hat{\sigma}^z}e^{-i\frac{\pi}{8}\hat{\sigma}^y}|\uparrow\rangle$ on every site. In first optimization phases, disentanglers are removed (set to 1), i.e., Trotterized tree tensor networks (TTN) [75, 76] are optimized. The resulting state is used to initialize the TMERA optimization. (b) Energy accuracy of optimized TMERA and fMERA as a function of the field strength g. Local minima are avoided by scanning from g=1.25 to g=0.75 and back. Especially in the paramagnetic phase (g>1) and at the critical point g=1, the accuracy of the fMERA is recovered with only t=2 Trotter steps per tensor.

of qubits need to be acted upon with the unitary gates. Specifically, when evaluating expectation values or gradients, as we progress from layer to layer, only the qubits inside the causal cone need to be in the interacting region of the quantum processor. The qubits that correspond to contraction lines which leave the causal cone as well as the auxiliary qubits, that are added to exploit translation invariance, can be shuttled out of the quantum register. When proceeding with the next layer, new qubits initialized in $|0\rangle$ to realize the isometries and new auxiliary qubits are shuttled in as indicated in Fig. 1b. Such shuttling has been demonstrated in ion-trap systems [49–51]. While the total number of required qubits is logarithmic in the system size, the required size of the processor register is system-size independent, e.g., 4q qubits for 1D binary MERA, 4q for 1D ternary MERA, and 14q for the 2D $2 \times 2 \mapsto 1$ MERA of Ref. [37].

VII. BENCHMARK SIMULATIONS AND SCANNING

To demonstrate and benchmark TMERA, we simulate the 1D transverse-field Ising model

$$\hat{H} = -\sum_{i} \hat{\sigma}_{i}^{x} \hat{\sigma}_{i+1}^{x} + g \sum_{i} \hat{\sigma}_{i}^{z}.$$
 (5)

The model has a critical point at g=1 with the paramagnetic phase for g>1 and the ferromagnetic phase for g<1. Fig. 2 shows results for homogeneous TMERA with the modified binary network structure [34], using an L-BFGS optimization. The TMERA energy densities e are compared to the exact infinite-system value $e_{\rm gs}^{\infty}$. The left panel shows the convergence for g=1.25, which

quickly reaches a high accuracy. The right panel, shows TMERA accuracies for $0.75 \le g \le 1.25$. Local minima are avoided through scanning, i.e., starting at g=1.25, g is lowered in steps, and the converged TMERA of the previous step is used to initialize the optimization of the next. Upon reaching g=0.75, we start scanning back to g=1.25. The numerical results confirm that a few Trotter steps t are sufficient to reach accuracies comparable to a full (non-Trotterized) MERA. In particular, t=2 gives already excellent results for $\chi=2^3$.

For the experimental implementation, the Trotter gates can be expressed in the CAN representations. Fig. 3 shows distributions of the rotation angles in the converged TMERA at different g. They are peaked at small angles. This remains true even for the critical point g=1. The fact that most angles are small implies that the required quantum computation times are correspondingly short because the rotations are implemented through time evolution.

VIII. DISCUSSION

The presented TMERA quantum eigensolver allows for the approximation of many-body ground states with numbers of qubits and time costs that increase only (square-)logarithmically in the system size and, as suggested by numerical tests, poly-logarithmically in the MERA bond dimension χ . The appendices provide details on the computational complexity for different MERA network structures (Appx. A), realization of layer-transition maps for homogeneous TMERA (Appx. B), optimization methods (Appx. C), and influence of different Trotter gate parametrizations (Appx. D).

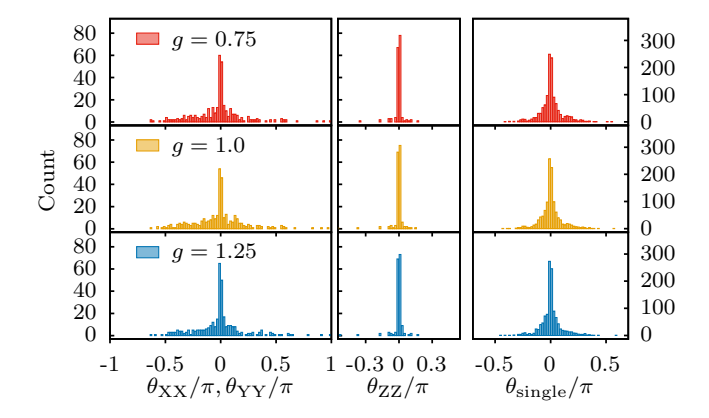


FIG. 3. Angle distribution in converged TMERA. Trotter gates can be parametrized in the canonical (CAN) form based on four single-qubit rotations and three Ising-interaction gates (XX, YY, and ZZ). All angles are found to be peaked around 0, which is favorable for the experimental realization. The plots show angle distributions for converged TMERA from Fig. 2 with t=2 Trotter steps.

The DMERA states of Ref. [77] form a subclass of TMERA. In a DMERA, the number of Trotter steps Din each layer is directly linked to the width $\sim 2D$ of the causal cone. The TMERA that we consider here have more structure, which allows us to tune these quantities independently, and the imposed structure admits a more direct comparison with the typical MERA used in classical simulations. The optimization based on the simultaneous perturbation stochastic approximation (SPSA), suggested in Ref. [77], is considerably less efficient because the energy derivative is only evaluated along random directions in the high-dimensional search space. Our gradient-based approach and the described utilization of translation invariance can be applied for any TMERA, including DMERA. Conversely, the robustness to noise as analyzed in Ref. [77] also applies generally to TMERA.

The decomposition of the MERA tensors into layers of nearest-neighbor Trotter gates is natural but not necessary. In future research, one could explore other network topologies to leverage, e.g., the all-to-all connectivity of ion-trap systems [78, 79] and to increase the expressiveness of TMERA at fixed cost. One could also consider other gate types, especially those that are naturally available in prominent quantum-computing architectures. An example are multi-qubit Mølmer-Sørensen gates [80, 81]. For an implementation on present-day devices, small two-qubit rotation angles are desirable. Hence, it will be interesting to explore how the angles and the TMERA accuracy are affected by adding large-angle penalty terms to the energy functional.

ACKNOWLEDGMENTS

We gratefully acknowledge helpful discussions with Christopher R. Monroe, Jungsang Kim, Sarah Brandsen, and Yikang Zhang, and support through US Department of Energy grant DE-SC0019449.

Appendix A: Computational complexity for 1D and 2D MERA

Let us discuss the quantum computational complexity for different TMERA in one and two dimensions and compare to the corresponding classical simulation costs. Fig. 4 shows the considered MERA networks: the 1D binary MERA, a modified 1D binary MERA [34], the 1D ternary MERA, a 2D $2 \times 2 \mapsto 1$ MERA [37], and a 2D $3 \times 3 \mapsto 1$ MERA [59]. We use the following labels:

- b denotes the MERA branching ratio.
- \bullet T denotes the number of layers.
- $\tau = 1, ..., T$ labels layers with layer $\tau = 1$ acting on the physical sites, i.e., τ increases in a renormalization step.
- $\chi = 2^q$ denotes the bond dimension with q being the corresponding number of qubits per renormalized site.
- A denotes the cross section of the causal cone for local operators, defined as the maximum number of renormalized sites inside the causal cone at any layer interface ($\tau \to \tau \pm 1$).
- t denotes the number of Trotter steps for each tensor in TMERA (or an upper bound).

For heterogeneous MERA, the total number of sites is denoted by N and assumed to be $\sim b^T$.

A.1. Classical time complexity

The costs for optimizing MERA on classical computers are determined by the cost of computing the so-called environment of a tensor. This is in turn determined by the cost of applying a renormalization step $(\tau \mapsto \tau + 1)$ to a local interaction term or, equivalently, for propagating a reduced density matrix inside the causal cone in the preparation direction $(\tau \mapsto \tau - 1)$. In each step, one needs to contract the tensors of disentanglers and isometries and trace out sites that leave the causal cone. The costs for these operations, which one obtains by optimizing the contraction sequence, are given in Table I. Generally speaking, it is favorable to have a narrow causal cone, which explains why the classical costs for the 1D modified binary and ternary MERA are smaller than those of the plain binary MERA. On the other hand, for a given bond dimension χ , the binary MERA can encode more entanglement than the other two 1D MERA types and may achieve higher accuracy.

The costs shown in Table I refer to one evaluation of the global energy gradient on a classical computer, or equivalently, a single update of all tensors in the Evenbly-Vidal algorithm [59]. For a homogeneous MERA, this

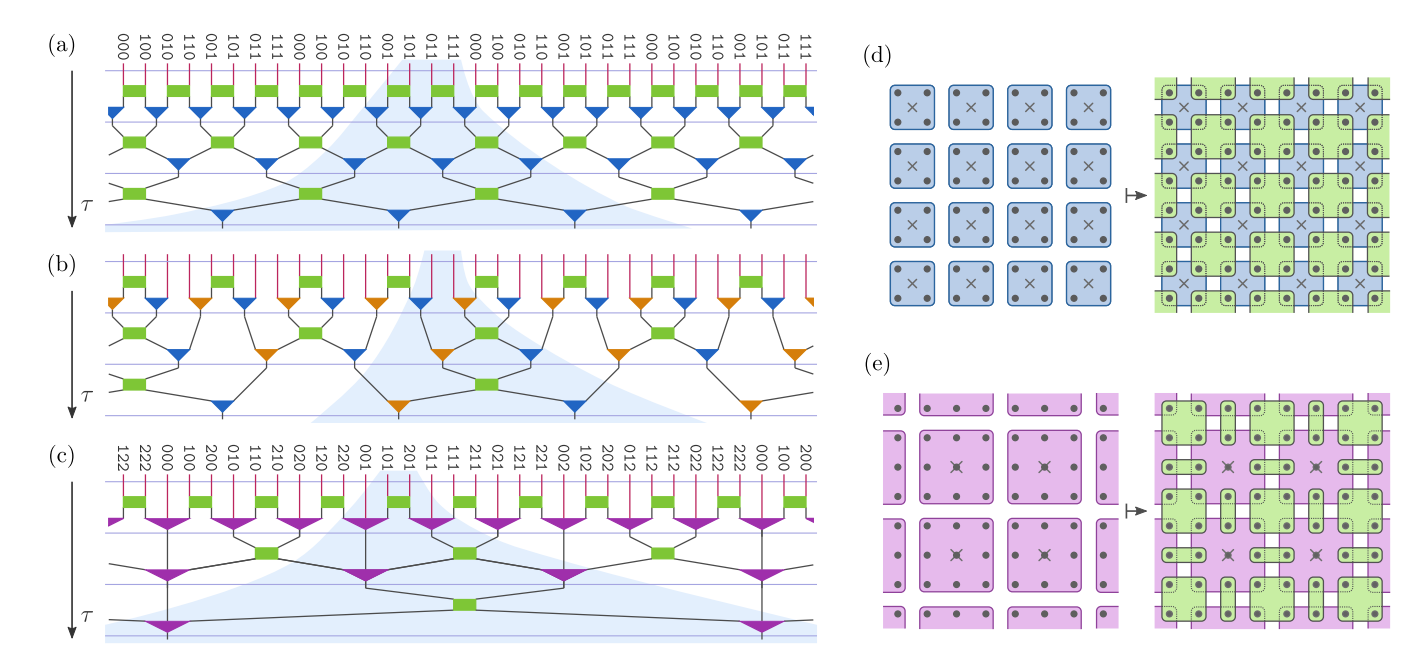


FIG. 4. **1D** and **2D** MERA tensor networks. Panels (a-c) each show three layers of a 1D MERA, where the preparation direction (decreasing τ) is upwards and causal cones for local operators are indicated: (a) the 1D binary MERA, (b) a modified 1D binary MERA [34], and (c) the 1D ternary MERA. Panels (d) and (e) each show one layer of a 2D MERA, where we progress in the preparation direction (decreasing τ) from left to right. (d) For the shown 2D $2 \times 2 \mapsto 1$ MERA [37], isometries map a renormalized sites (crosses) into blocks of 2×2 sites (dots) before disentanglers are applied to shifted 2×2 site blocks. (e) For the shown 2D $3 \times 3 \mapsto 1$ MERA [59], isometries map a renormalized sites (crosses) into blocks of 3×3 sites (dots) before one applies 4-site and two 2-site disentanglers.

cost, like the number of different tensors, is linear in T. For heterogeneous MERA, the total number of tensors and the cost are proportional to $\sum_{\tau=1}^T b^{\tau} \sim N$. The table shows the classical costs for fMERA because there is not much to gain by exploiting the Trotter structure of TMERA tensors unless one is willing to introduce approximations.

A.2. Quantum computation time complexity

For the hybrid quantum-classical TMERA algorithm, the width of the causal cone is not as decisive for the computation costs. It determines primarily the number of qubits that need to be simultaneously in the interaction zone of the computer. Also, the specific network structure inside the cone, which influences the classical contraction costs, does not affect the scaling of the quantum computation costs. As discussed in Sec. III, the quantum costs for evaluating the TMERA expectation value of a local interaction term \hat{h}_i is proportional to tT. For homogeneous TMERA, the expectation value of the entire Hamiltonian $\hat{H} = \sum_{i} \hat{h}_{i}$ can in fact be evaluated in one go, i.e., with time $\mathcal{O}(tT)$. As there are $\mathcal{N} = \mathcal{O}(qtT)$ different Trotter gates, one needs $\mathcal{O}(q(tT)^2)$ time to evaluate the energy gradient. For heterogeneous TMERA, there are $\mathcal{N} = \mathcal{O}(qtN)$ different Trotter gates with $\mathcal{O}(qtN/b^{\tau})$ located in layer τ . To evaluate the gradient with respect to one Trotter gate in layer τ , we need to evaluate the $\mathcal{O}(b^{\tau})$ expectation values for all local interactions terms that it affects. Hence, one needs $\sum_{\tau=1}^T \mathcal{O}(tT\,b^{\tau}\,qtN/b^{\tau}) = \mathcal{O}(q(tT)^2N)$ time for the gradient evaluation of heterogeneous TMERA. For the comparison to the classical computation costs (Sec. A.1), our benchmark simulations suggest that the accuracy of the $\chi=2^q$ fMERA is recovered when choosing the number of Trotter steps t proportional to q^{α} with a model-specific exponent $\alpha\geq 1/D$, where D is the number of spatial dimensions.

The classical component of the hybrid TMERA eigensolver controls the gradient evaluation and steers the gradient-based energy minimization. Its time complexity is always subleading to the quantum time complexity: For a TMERA with $\mathcal N$ different Trotter gates, the classical component operates on a vector space of dimension $\mathcal O(\mathcal N)$. The classical time complexity for one iteration of gradient descent or L-BFGS is just $\mathcal O(\mathcal N)$.

Although it is much less efficient than TMERA, one can also optimize fMERA using a quantum computer. A disentangler that acts on n renormalized sites can be decomposed exactly into a circuit of $\mathcal{O}(2^{2nq})$ single-qubit and CNOT gates [55–57]. An exact representation of an isometry that maps n sites into m > n requires $\mathcal{O}(2^{(n+m)q})$ single-qubit and CNOT gates [58]. The time cost for the energy gradient evaluation of a homogeneous fMERA is then obtained by squaring the largest number of gates per tensor and multiplying by T^2 .

MERA type	Properties		Number of qubits			Times, homogeneous			Times, heterog.	
	b	A	total	reg.	aux.	classical	quantum	f-quantum	classical	quantum
1D binary	2	3	$\sim 3qT$	4q	T	$\mathcal{O}(2^{9q}T)$	$\mathcal{O}(q(tT)^2)$	$\mathcal{O}(2^{8q}T^2)$	$\mathcal{O}(2^{9q}N)$	$\mathcal{O}(q(tT)^2N)$
1D mod. binary	2	2	$\sim 2qT$	3q + 1	2T	$\mathcal{O}(2^{7q}T)$	$\mathcal{O}(q(tT)^2)$	$\mathcal{O}(2^{8q}T^2)$	$\mathcal{O}(2^{7q}N)$	$\mathcal{O}(q(tT)^2N)$
1D ternary	3	2	$\sim 4qT$	4q	2T	$\mathcal{O}(2^{8q}T)$	$\mathcal{O}(q(tT)^2)$	$\mathcal{O}(2^{8q}T^2)$	$\mathcal{O}(2^{8q}N)$	$\mathcal{O}(q(tT)^2N)$
$2D \ 2 \times 2 \mapsto 1$	4	3×3	$\sim 27qT$	14q	2T	$\mathcal{O}(2^{28q}T)$	$\mathcal{O}(q(tT)^2)$	$\mathcal{O}(2^{16q}T^2)$	$\mathcal{O}(2^{28q}N)$	$\mathcal{O}(q(tT)^2N)$
$2D \ 3 \times 3 \mapsto 1$	9	2×2	$\sim 32qT$	15q	4T	$\mathcal{O}(2^{16q}T)$	$\mathcal{O}(q(tT)^2)$	$\mathcal{O}(2^{16q}T^2)$	$\mathcal{O}(2^{16q}N)$	$\mathcal{O}(q(tT)^2N)$

TABLE I. Computational complexity. For the five 1D and 2D MERA network structures shown in Fig. 4, this table states the number of qubits needed for the variational quantum eigensolver and compares the time complexity for the quantum evaluation of energy gradients to that in the classical algorithms. Columns 2 and 3 show the branching ratio b and the cross section A of the causal cone for local operators like the considered Hamiltonian interaction terms. Columns 4–6 show the total number of qubits needed, the number of qubits needed in the quantum processor register, and the number of auxiliary qubits needed for the time efficient processing of homogeneous MERA. Columns 7–9 concern homogeneous MERA. Column 7 shows the classical computation times for fMERA, which agree with those for TMERA as, on a classical computer, the Trotter structure of tensors does not admit substantial gains. Columns 8 and 9 show the quantum computation times for TMERA and fMERA. The TMERA accuracy is expected to approach the fMERA accuracy for $t \propto q^{\alpha}$. Columns 10 and 11 show the classical and the quantum computation times for heterogeneous TMERA.

A.3. Quantum space complexity

In every layer transition $\tau \mapsto \tau - 1$, (b-1)Aq further qubits, initialized in the reference state $|0\rangle$, need to be introduced to realize the isometries. For a TMERA with T layers, one hence needs a total of $\sim (b-1)AqT$ qubits.

Not all of these qubits need to be simultaneously present in the interaction region (register) of the quantum processor. In fact, after (or during) a layer transition, (b-1)Aq entangled qubits can be moved out of the register and will not need to interact again. In this paragraph, let us consider an architecture with a quantum register and a write-only memory, in the sense that qubits can be moved from the register to the memory but are never retrieved, and new qubits (initialized in $|0\rangle$) can be moved into the register. This is a likely set up for early-stage ion-trap quantum computers with ion shuttling [49–51]. The number of qubits needed in the register is primarily determined by the cross section A of the causal cone. More precisely, from the sequence of contractions inside each layer of the causal cone, one can determine how many renormalized sites (groups of q qubits) need to be inside the interaction region at any point in time. One can reduce this number by not insisting on parallel execution of gates, but shifting the MERA tensors of a layer-transition map temporally so that some qubits can be moved out of the interaction region before other $|0\rangle$ qubits are moved in. The results for the considered MERA networks are shown in Table I.

As discussed in Sec. V, a major computation time reduction for the homogeneous MERA is achieved by adding auxiliary qubits in order to take appropriate convex combinations of the layer-transition maps like \hat{U}_L and \hat{U}_R such that the energy density for the full (infinite) system is obtained in one go. The number of auxiliary qubits needed is proportional to \log_2 of the number of transition maps. These qubits can also be moved from the register into memory after the layer-transition step.

Appendix B: Layer transition maps for homogeneous MERA

Let us discuss in more detail, how auxiliary qubits can be applied to realize convex combinations of layer-transition maps in the preparation. In this way, the spatially averaged A-site density matrices of homogeneous TMERA can be prepared on the quantum computer in $\mathcal{O}(tT)$ time. Hence, the energy density or a component of the energy gradient can be obtained in $\mathcal{O}(tT)$ time.

B.1. 1D binary MERA

This case was already discussed shortly in Sec. V. For the 1D binary MERA, local operators have causal cones of width A=3. The sequence of layer-transition maps \hat{U}_L and \hat{U}_R for the causal cone of sites

$$\mathcal{A}_i := \{i, \dots, i + A - 1\} \tag{B1}$$

on the physical lattice can be deduced from the binary representation $i_1i_2i_3...$ of i with $i_{\tau} \in \{0,1\}$, where i_1 is the least significant bit. For the choice shown in Figs. 4a and 5a, $i_{\tau} = 0$ or 1 means that we progress from layer τ to layer $\tau - 1$ by applying transition map $\hat{U}_L \equiv \hat{U}_0$ or $\hat{U}_R \equiv \hat{U}_1$, respectively. Specifically, the causal-cone state for sites \mathcal{A}_i reads

$$|\Psi_i\rangle = \hat{U}_{i_1} \cdots \hat{U}_{i_T} (|T\rangle^{\otimes A}),$$
 (B2)

where state $|T\rangle$ for a single renormalized site defines the so-called top tensor of the MERA. Here and in the following, we do not explicitly denote the τ dependence of the layer-transition maps and use the convention that operators act on the A active sites in the causal cone and the remaining inactive sites are left untouched as indicated in Fig. 5b.

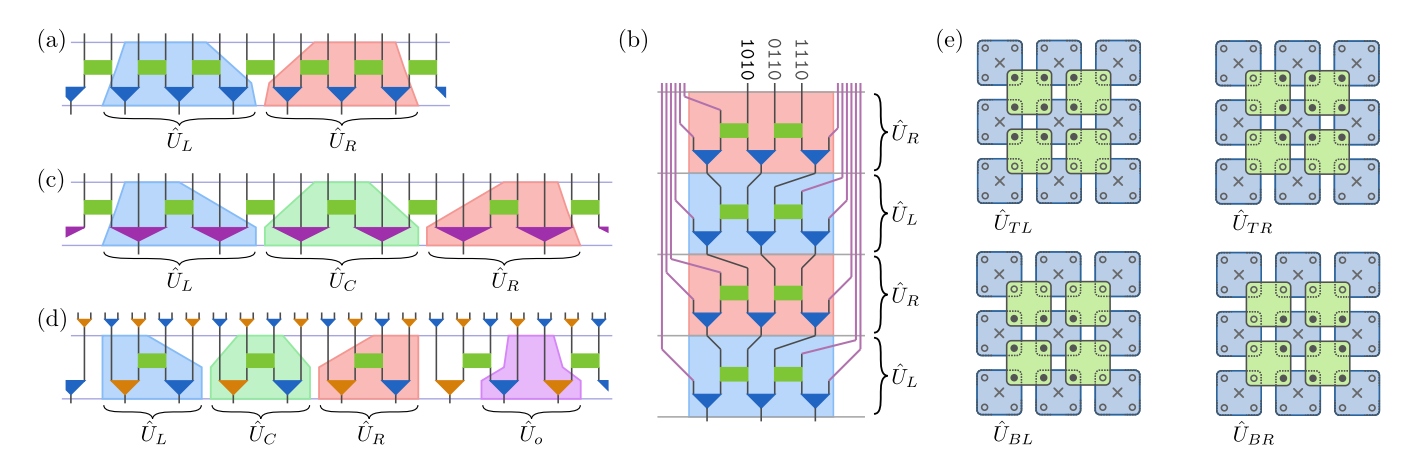


FIG. 5. Layer transition maps. (a) The 1D binary MERA has causal-cone width A=3 and two layer-transition maps \hat{U}_L and \hat{U}_R . Panel (b) gives an example for the sequence of transition maps in a particular causal cone, here, in correspondence with Fig. 4a. For the binary MERA, the sequence can be determined from the binary representation of the index (four least significant digits shown) with 0 corresponding to \hat{U}_L and 1 to \hat{U}_R . (c) The 1D ternary MERA has A=2 and three transition maps \hat{U}_L , \hat{U}_C , and \hat{U}_R . (d) The 1D modified binary MERA has A=2 and one needs to distinguish even and odd bonds. Transition maps \hat{U}_L and \hat{U}_R map from even to odd bonds, \hat{U}_C from an even bond, and \hat{U}_O from an odd to an even bond. (e) The 2D $2 \times 2 \mapsto 1$ MERA [37] has $A=3 \times 3$ and four layer-transition maps \hat{U}_{TL} , \hat{U}_{TR} , \hat{U}_{BL} , and \hat{U}_{BR} . The renormalized causal-cone sites $\mathcal{A}_i^{(\tau)}$ that the maps act on are indicated by crosses, the sites that leave the causal cone during/after the map are indicated by empty circles, and the sites $\mathcal{A}_i^{(\tau-1)}$ that remain in the causal-cone after the preparation step are indicated by filled circles. The layer-transition maps differ in the positions of the latter.

For quantities like the energy density, we wish to evaluate the spatial average $\hat{\rho} = \frac{1}{N} \sum_i \hat{\rho}_i$ of the reduced density matrices $\hat{\rho}_i := \operatorname{Tr}_{\mathcal{A}_i^{\perp}} |\Psi_i\rangle \langle \Psi_i|$ for the blocks of sites \mathcal{A}_i . The partial trace is over the inactive sites (outside the causal cone) and will not be denoted explicitly in the following. Starting from $\hat{\rho}^{(T)} := (|T\rangle \langle T|)^{\otimes A}$, we can recursively define

$$\hat{\rho}^{(\tau-1)} = \frac{1}{2} \sum_{i} \hat{U}_{i_{\tau}} \hat{\rho}^{(\tau)} \hat{U}_{i_{\tau}}^{\dagger}$$
 (B3a)

such that

$$\hat{\rho}^{(0)} = \frac{1}{2^T} \sum_{i_1, \dots, i_T} \hat{U}_{i_1} \cdots \hat{U}_{i_T} \hat{\rho}^{(T)} \hat{U}_{i_T}^{\dagger} \cdots \hat{U}_{i_1}^{\dagger} = \hat{\rho}. \quad (B3b)$$

 \hat{U}_L and \hat{U}_R are related to each other by a site permutation. Hence, the quantum channel (B3a) can be implemented through a Stinespring dilation [73, 74] with a single auxiliary qubit per layer. The auxiliary qubit is initialized in the state $(|0\rangle + |1\rangle)/\sqrt{2}$ and used for a controlled site permutation such that, after tracing out the auxiliary qubit, one obtains the channel (B3a).

B.2. 1D ternary MERA

We can proceed along the same lines for the 1D ternary MERA. The only modifications are due to, now, having the three transition maps $\hat{U}_L \equiv \hat{U}_0$, $\hat{U}_C \equiv \hat{U}_1$, and $\hat{U}_R \equiv \hat{U}_2$ shown in Fig. 5c. Correspondingly, we now use the ternary representation $i_1 i_2 i_3 \dots$ of the site index

i with $i_{\tau} \in \{0,1,2\}$ and replace the prefactors 1/2 in Eqs. (B3) by 1/3. For the Stinespring dilation, we now require two auxiliary qubits per layer, which are, for example, initialized in the state $(|0,0\rangle + |1,0\rangle + |0,1\rangle)/\sqrt{3}$ to perform the controlled site permutations that relate the three unitaries $\hat{U}_{i_{\tau}}$.

B.3. 2D $2 \times 2 \mapsto 1$ MERA

Also the 2D $2 \times 2 \mapsto 1$ MERA can be treated similarly. Now, we use binary representations $x_1x_2x_3...$ and $y_1y_2y_3...$ for the x and y coordinates of site i on the square lattice with $x_{\tau}, y_{\tau} \in \{0, 1\}$. There are four layer-transition maps $\hat{U}_{TL} \equiv \hat{U}_{0,0}$, $\hat{U}_{TR} \equiv \hat{U}_{1,0}$, $\hat{U}_{BL} \equiv \hat{U}_{0,1}$, $\hat{U}_{BR} \equiv \hat{U}_{1,1}$, where \hat{U}_{TL} corresponds to the causal cone continuing along the inner (top-left corner) 3×3 square indicated in Fig. 5e. The layer-transition channel reads

$$\hat{\rho}^{(\tau-1)} = \frac{1}{4} \sum_{x_{\tau}, y_{\tau}} \hat{U}_{x_{\tau}, y_{\tau}} \hat{\rho}^{(\tau)} \hat{U}_{x_{\tau}, y_{\tau}}^{\dagger}.$$
 (B4)

Its Stinespring dilation can be implemented with two auxiliary qubits, each initialized in $(|0\rangle+|1\rangle)/\sqrt{2}$, to realize the controlled site permutations that relate the maps $\hat{U}_{x_{\tau},y_{\tau}}$ to each other. The first auxiliary qubit can be used to permute rows of sites and the second to permute columns of sites on the inner 4×4 square in Fig. 5e.

B.4. 1D modified binary MERA

The cases of the 1D modified binary MERA and the 2D $3 \times 3 \mapsto 1$ MERA are bit more involved.

First note that the layer-transition channel (B3a) for the (unmodified) 1D binary MERA can also be explained as follows: Let $\mathcal{A}_i^{(\tau)}$ denote the block of renormalized sites $\{i,\ldots,i+A-1\}$ after τ renormalization steps, i.e., at the interface of layers τ and $\tau+1$; $\mathcal{A}_i^{(0)}$ agrees with the block \mathcal{A}_i of physical sites in Eq. (B1). Let $\hat{\rho}_i^{(\tau)}$ denote the reduced density matrix for $\mathcal{A}_i^{(\tau)}$, constructed from all MERA tensors in the causal cone of $\mathcal{A}_i^{(\tau)}$ which ranges from layer $\tau+1$ to the final layer T. Given all density matrices $\hat{\rho}_i^{(\tau)}$ for layer τ , we want to compute those for layer $\tau-1$. The density matrices $\hat{\rho}_j^{(\tau-1)}$ and $\hat{\rho}_{j+1}^{(\tau-1)}$ for the two blocks $\mathcal{A}_j^{(\tau-1)}$ and $\mathcal{A}_{j+1}^{(\tau-1)}$ whose causal cones contain $\mathcal{A}_i^{(\tau)}$, are obtained by conjugating $\hat{\rho}_i^{(\tau)}$ with the appropriate layer- τ transition maps

$$\hat{\rho}_{j}^{(\tau-1)} = \hat{U}_{L} \hat{\rho}_{i}^{(\tau)} \hat{U}_{L}^{\dagger} \quad \text{and} \quad \hat{\rho}_{j+1}^{(\tau-1)} = \hat{U}_{R} \hat{\rho}_{i}^{(\tau)} \hat{U}_{R}^{\dagger}. \quad (B5)$$

Now, the spatially averaged density matrix $\hat{\rho}^{(\tau-1)} = \frac{b^{\tau-1}}{N} \sum_{j} \hat{\rho}_{j}^{(\tau-1)}$ is obtained by averaging over all sites i in layer τ and the two corresponding sites in layer $\tau-1$. Thus, we recover Eq. (B3a).

The 1D modified binary MERA with A=2 can be addressed similarly. In this case, not all bonds are equivalent. Depending on whether we are on an even or an odd bond, we either apply one of the three layer-transition maps $\hat{U}_L, \hat{U}_C, \hat{U}_R$ or the map \hat{U}_o , respectively, as shown in Fig. 5d. While \hat{U}_L and \hat{U}_R move the causal cone from an even to an odd bond, \hat{U}_C maps from an even to an even bond, and \hat{U}_o maps from an odd to an even bond. Let $\hat{\rho}_e^{(\tau)}$ denote the bond density matrix averaged over all even bonds for layer τ and $\hat{\rho}_o^{(\tau)}$ the average over all odd bonds. Then, the same considerations as above lead to the layer transitions

$$\hat{\rho}_{e}^{(\tau-1)} = \frac{1}{2} \left(\hat{U}_{C} \hat{\rho}_{e}^{(\tau)} \hat{U}_{C}^{\dagger} + \hat{U}_{o} \hat{\rho}_{o}^{(\tau)} \hat{U}_{o}^{\dagger} \right), \tag{B6a}$$

$$\hat{\rho}_{o}^{(\tau-1)} = \frac{1}{2} \left(\hat{U}_{L} \hat{\rho}_{e}^{(\tau)} \hat{U}_{L}^{\dagger} + \hat{U}_{R} \hat{\rho}_{e}^{(\tau)} \hat{U}_{R}^{\dagger} \right). \tag{B6b}$$

For the evaluation of energy densities and gradients we want to prepare the spatially averaged density matrices $\hat{\rho}_e^{(0)}$ and $\hat{\rho}_o^{(0)}$ for even and odd bonds of the physical lattice. To realize this, we can introduce an additional flag qubit in the register of the quantum computer which indicates whether we are on an even or odd bond, i.e., progressing in the preparation direction, we want to prepare the states

$$\hat{\rho}^{(\tau)} := \frac{1}{2} \left(|0\rangle \langle 0|_f \otimes \hat{\rho}_e^{(\tau)} + |1\rangle \langle 1|_f \otimes \hat{\rho}_o^{(\tau)} \right).$$
 (B7)

For these, the layer-transition channel reads

$$\hat{\rho}^{(\tau-1)} = \frac{1}{2} \sum_{k=1}^{4} \hat{L}_k \hat{\rho}^{(\tau)} \hat{L}_k^{\dagger} \quad \text{with}$$

$$\hat{L}_1 = |0\rangle \langle 0|_f \otimes \hat{U}_C, \quad \hat{L}_2 = |0\rangle \langle 1|_f \otimes \hat{U}_o$$

$$\hat{L}_3 = |1\rangle \langle 0|_f \otimes \hat{U}_L, \quad \hat{L}_4 = |1\rangle \langle 0|_f \otimes \hat{U}_R.$$
(B8)

It can be implemented by a Stinespring dilation that employs two auxiliary qubits per layer as specified in the second row of Table I.

Appendix C: Gradient evaluation and Riemannian optimization

The goal of the variational quantum eigensolver is to minimize the energy expectation value $E = \langle \Psi | \hat{H} | \Psi \rangle$ over a TMERA variety $\{ | \Psi \rangle \}$, where the TMERA is characterized by the network structure, bond dimensions, and the tensor Trotterization as previously discussed. This minimization can be carried out by evaluating energy gradients and employing them in gradient descent methods or, preferably, quasi-Newton methods like the limited-memory Broyden–Fletcher–Goldfarb–Shanno (L-BFGS) algorithm [62, 63].

C.1. Gradients in the CNOT and CAN parametrizations

In the CNOT and CAN parametrizations, the Trotter gates are expressed in terms of single and two-qubit rotations $\hat{R}_{\hat{\sigma}}(\theta) = e^{-\mathrm{i}\theta\hat{\sigma}/2}$ [Eq. (1)]. The rotation angles θ parametrize the TMERA variety. To compute the energy derivative for one of these angles, we can write the energy expectation value in the form $E(\theta) = \text{Tr}(\hat{A}\hat{R}_{\hat{\sigma}}^{\dagger}(\theta)\hat{B}\hat{R}_{\hat{\sigma}}(\theta))$, where the Hermitian operators \hat{A} and \hat{B} comprise the remaining tensors of $\langle \Psi |, |\Psi \rangle$, and the Hamiltonian. The derivative is

$$\partial_{\theta} E(\theta) = \frac{i}{2} \operatorname{Tr} \left(\hat{A} \hat{R}_{\hat{\sigma}}^{\dagger}(\theta) [\hat{\sigma}, \hat{B}] \hat{R}_{\hat{\sigma}}(\theta) \right).$$
 (C1)

For the Hermitian and unitary operators $\hat{\sigma}$, $\hat{R}_{\hat{\sigma}}(\pm \frac{\pi}{2}) = (1 \mp i\hat{\sigma})/\sqrt{2}$ and, hence,

$$i[\hat{\sigma}, \hat{B}] = \hat{R}_{\hat{\sigma}}^{\dagger}(\frac{\pi}{2})\hat{B}\hat{R}_{\hat{\sigma}}(\frac{\pi}{2}) - \hat{R}_{\hat{\sigma}}^{\dagger}(-\frac{\pi}{2})\hat{B}\hat{R}_{\hat{\sigma}}(-\frac{\pi}{2}). \quad (C2)$$

such that Eq. (2) follows. In this way, the gradient can be evaluated on the quantum computer by measuring energy expectation values [82, 83].

For homogeneous TMERA, the same rotation occurs multiple times as tensors are repeated in the translation-invariant MERA layers. Applying the product rule, this just means that the derivative $\partial_{\theta} E$ will contain one term for each occurrence of the rotation $\hat{R}(\theta)$. This sum can be evaluated efficiently as described in the main text and Appx. B.

With the gradient in hand, one can apply standard implementations of gradient descent or quasi-Newton methods like L-BFGS.

C.2. An alternative Riemannian version of the optimization

Instead of employing an explicit parametrization of the Trotter gates, one can formulate the problem as a minimization over the manifold

$$\mathcal{M} := \mathrm{U}(4)^{\times \mathcal{N}} \tag{C3}$$

formed by the product of the unitary groups for the \mathcal{N} Trotter gates of the TMERA. For homogeneous TMERA, repeated gates are counted once. This Riemannian approach turns out to have somewhat improved convergence properties as discussed in Appx. D. Note that one can take unitary gauge freedoms on the inputs of the Trotter gates into account and consider quotient groups $U(4)/(U(2) \times U(2))$. For the simplicity of notation, we stick to the full U(4) in the following.

For the optimization, we can regard \mathcal{M} as embedded in the Euclidean space

$$\mathcal{E} = \operatorname{End}(\mathbb{C}^4)^{\times \mathcal{N}} \simeq \mathbb{R}^{32\mathcal{N}},$$
 (C4)

which is the space of the Trotter gates without the unitarity constraint. Let $u \in \mathcal{M} \subset \mathcal{E}$ denote the vector that contains the matrix elements of all gates and $E(u) = \langle \Psi(u) | \hat{H} | \Psi(u) \rangle$ the energy functional. To apply gradient-based optimization algorithms in this setting, we need to compute the derivative $\partial_u E(u)$, project it onto the tangent space \mathcal{T}_u of \mathcal{M} at u to obtain the gradient direction, construct retractions for line search, and vector transport to be able to sum gradient vectors from different points on the manifold. This is the program of Riemannian optimization as discussed generally in Refs. [84, 85] and recently demonstrated for MERA in Refs. [86, 87].

In the following, consider a single unitary $\hat{u} \in \mathrm{U}(n)$ and the inner product $(\hat{u}, \hat{u}') := \mathrm{Re} \, \mathrm{Tr}(\hat{u}^{\dagger} \hat{u}')$. The extension to the product manifold \mathcal{M} is straightforward. As in Eq. (C1), let us write the energy expectation value in the form

$$E(\hat{u}) = \langle \Psi(\hat{u}) | \hat{H} | \Psi(\hat{u}) \rangle = \text{Tr}(\hat{A}\hat{u}^{\dagger} \hat{B}\hat{u}).$$
 (C5)

Then, the energy gradient in the embedding space $\operatorname{End}(\mathbb{C}^n)$ is

$$\hat{d} = 2\hat{B}\hat{u}\hat{A} \tag{C6}$$

such that $\partial_{\varepsilon} E(\hat{u} + \varepsilon \hat{w})|_{\varepsilon=0} = (\hat{d}, \hat{w})$ for all \hat{w} . An element \hat{w} of the tangent space $\mathcal{T}_{\hat{u}}$ for U(n) at \hat{u} needs to obey $(\hat{u} + \varepsilon \hat{w})^{\dagger}(\hat{u} + \varepsilon \hat{w}) = \mathbb{1} + \mathcal{O}(\varepsilon^2)$, i.e., $\hat{u}^{\dagger}\hat{w} + \hat{w}^{\dagger}\hat{u} = 0$. So, $\hat{u}^{\dagger}\hat{w}$ needs to be skew-Hermitian and, hence,

$$\mathcal{T}_{\hat{u}} = \{ i \hat{u} \hat{\eta} \mid \hat{\eta} = \hat{\eta}^{\dagger} \in \text{End}(\mathbb{C}^n) \}. \tag{C7}$$

The Riemannian energy gradient \hat{g} for the manifold U(n) at \hat{u} is obtained by projecting \hat{d} onto the tangent space such that $(\hat{w}, \hat{g}) = (\hat{w}, \hat{d})$ for all $\hat{w} \in \mathcal{T}_{\hat{u}}$. This gives

$$\hat{g} = (\hat{d} - \hat{u}\hat{d}^{\dagger}\hat{u})/2 \in \mathcal{T}_{\hat{u}}. \tag{C8}$$

For a line search on the manifold, we need a retraction, i.e., a curve $\hat{r}_{\hat{u},\hat{p}}(\tau)$ on the manifold that starts from $\hat{u} = \hat{r}_{\hat{u},0}$ in direction $\hat{p} = \partial_{\tau}\hat{r}_{\hat{u},\hat{p}}(\tau)|_{\tau=0} \in \mathcal{T}_{\hat{u}}$. We use

$$\hat{r}_{\hat{u},\hat{p}}(\tau) := e^{\tau \hat{p}\hat{u}^{\dagger}} \hat{u} \in U(n).$$
 (C9)

For quasi-Newton methods, we also need to compute differences of Riemannian gradients from different points on the manifold, specifically, for two points on a retraction. This is accomplished by vector transport, i.e., a map between the two corresponding tangent spaces. We use,

$$\hat{T}_{\hat{u},\hat{p}}(\tau)\hat{w} := e^{\tau\hat{p}\hat{u}^{\dagger}}\hat{w} \quad \text{for} \quad \hat{w} \in \mathcal{T}_{\hat{u}}, \ \tau \in \mathbb{R}$$
 (C10)

This gives an element of the tangent space at $\hat{r}_{\hat{u},\hat{p}}(\tau)$ and $\hat{T}_{\hat{u},0}\hat{w} = \hat{w}$. The vector transport is isometric in the sense that $\left(\hat{T}_{\hat{u},\hat{p}}(\tau)\hat{w},\hat{T}_{\hat{u},\hat{p}}(\tau)\hat{w}'\right) = (\hat{w},\hat{w}')$ for all $\hat{p},\hat{w},\hat{w}' \in \mathcal{T}_{\hat{u}}$ and $\tau \in \mathbb{R}$.

In analogy to Eq. (2), the Riemannian gradient (C8) can be obtained on the quantum computer by measuring energies of TMERA where one Trotter gate is modified: The tangent space $\mathcal{T}_{\hat{u}}$ is a real n^2 -dimensional vector space and we can choose a basis $\{i\hat{u}\hat{\sigma}_j \mid j=1,\ldots,n^2\}$ with Hermitian unitaries $\hat{\sigma}_j$, i.e., $\hat{\sigma}_j=\hat{\sigma}_j^{\dagger}$ and $\hat{\sigma}_j^2=\mathbb{1}$. For $n=2^q$, such a basis is given by the q-fold tensor products of the Pauli matrices $\{\mathbb{1},\hat{\sigma}^x,\hat{\sigma}^y,\hat{\sigma}^z\}$. With $(\hat{\sigma}_j,\hat{\sigma}_k)=\delta_{j,k}n$, we can expand the energy gradient in the form $\hat{g}=\mathrm{i}\sum_{j=1}^{n^2}\alpha_j\hat{u}\hat{\sigma}_j/n$ and evaluate the expansion coefficients α_j using the energy expectation values (C5),

$$\alpha_{j} = (\hat{g}, i\hat{u}\hat{\sigma}_{j}) = (\hat{d}, i\hat{u}\hat{\sigma}_{j}) = \operatorname{Re}\operatorname{Tr}(i\hat{d}^{\dagger}\hat{u}\hat{\sigma}_{j})$$

$$= -i\operatorname{Tr}\left(\hat{A}[\hat{\sigma}_{j}, \hat{u}^{\dagger}\hat{B}\hat{u}]\right)$$

$$= E\left(\hat{u}\hat{R}_{\hat{\sigma}_{j}}(-\frac{\pi}{2})\right) - E\left(\hat{u}\hat{R}_{\hat{\sigma}_{j}}(\frac{\pi}{2})\right). \tag{C11}$$

For the third line, we have used Eq. (C2) and $\hat{R}_{\hat{\sigma}}(\theta) = e^{-i\theta\hat{\sigma}/2}$.

To minimize TMERA energies, we can employ a Riemannian version of the L-BFGS algorithm. For the following, we return to the global optimization problem on the product manifold (C3) with the embedding space (C4), vectors $\mathbf{u} \in \mathcal{M}$ comprising the matrix elements of all Trotter gates, and the inner product $(\mathbf{u}, \mathbf{u}') = \operatorname{Re} \mathbf{u}^{\dagger}\mathbf{u}'$. Similarly, gradients \hat{g} , retractions \hat{r} etc. are now written in a vectorized form. In the Newton method, one generates a sequence of points $\mathbf{u}_1, \mathbf{u}_2, \dots \in \mathcal{M}$ that converge quadratically fast to a minimum of $E(\mathbf{u})$. In each step, one obtains a second-order model of $E(\mathbf{u})$ using the Riemannian gradient \mathbf{g}_k and the inverse Hessian H_k at \mathbf{u}_k . The vector $\mathbf{p}_k := -H_k \mathbf{g}_k \in \mathcal{T}_{\mathbf{u}_k}$ that points from \mathbf{u}_k to the minimum of the quadratic model is used for

```
1: \mathbf{u}_0 \in \mathcal{M}, \ \varepsilon > 0, \ \ell \in \mathbb{N}, \ 0 < c_1 < \frac{1}{2} < c_2 < 1, \ \gamma = 1, \ k = 0, \ m = 0
                                                                                                                                                                                                                                                \triangleright Initialization.
                                                                                                                               \triangleright Riemannian gradient g_k at u_k determined according to Eq. (C8).
  2: while ||g_k|| > \varepsilon do
               \boldsymbol{p}_k = -\boldsymbol{g}_k
                                                                                                                  \triangleright Lines 3-11 determine the search direction p_k = -\tilde{H}_k g_k with Eq. (C12).
  3:
                                                                                                                                      \triangleright Compute -V_m^{\dagger}V_{m+1}^{\dagger}\cdots V_{k-1}^{\dagger}\boldsymbol{g}_k and \xi_i := -(\boldsymbol{s}_i, V_i^{\dagger}\cdots V_{k-1}^{\dagger}\boldsymbol{g}_k).
                for i = k - 1, k - 2, ..., m do
  4:
                       \xi_i \leftarrow \rho_i(\boldsymbol{s}_i, \boldsymbol{p}_k)
  5:
  6:
                       \boldsymbol{p}_k \leftarrow \boldsymbol{p}_k - \xi_i \boldsymbol{y}_i
  7:
               end for
                                                                                                                                                               \qquad \qquad \triangleright \text{ Multiply with } \tilde{H}_{m-1} := \gamma \mathbb{1}. \triangleright \text{ Multiply with } V_{k-1} \cdots V_m \text{ and insert } \rho_i \boldsymbol{s}_i \boldsymbol{s}_i^{\dagger} \text{ terms.}
  8:
               \boldsymbol{p}_k \leftarrow \gamma \boldsymbol{p}_k
                for i = m, m + 1, ..., k - 1 do
  9:
10:
                       \boldsymbol{p}_k \leftarrow \boldsymbol{p}_k - \rho_i \boldsymbol{s}_i(\boldsymbol{y}_i, \boldsymbol{p}_k) + \boldsymbol{s}_i \xi_i
                end for
                                                                                                                                                                                                                                   \triangleright Now, \boldsymbol{p}_k = -\tilde{H}_k \boldsymbol{q}_k.
11:
                Do line search to find \tau_k \in \mathbb{R} that satisfies the Wolfe conditions. With u_{k+1} := r_{u_k, p_k}(\tau_k):
12:
13:
                          E(\boldsymbol{r}_{\boldsymbol{u}_k},\boldsymbol{p}_k(\tau_k)) \leq E(\boldsymbol{u}_k) + c_1 \tau_k(\boldsymbol{g}_k,\boldsymbol{p}_k),
14:
                          \partial_{\tau} E(\mathbf{r}_{\mathbf{u}_k,\mathbf{p}_k}(\tau))|_{\tau=\tau_k} \geq c_2 \partial_{\tau} E(\mathbf{r}_{\mathbf{u}_k,\mathbf{p}_k}(\tau))|_{\tau=0}.
                \boldsymbol{u}_{k+1} = \boldsymbol{r}_{\boldsymbol{u}_k, \boldsymbol{p}_k}(\tau_k)
                                                                                                                                                             \triangleright For the following, T_k := T_{u_k, p_k}(\tau_k) from Eq. (C10).
15:
                s_k = T_k \tau_k p_k, \quad y_k = g_{k+1} - T_k g_k, \quad \rho_k = 1/(s_k, y_k), \quad \gamma \leftarrow (s_k, y_k)/\|y_k\|^2
16:
                m \leftarrow \max(k - \ell, 0)
17:
                Discard (\rho_{m-1}, \boldsymbol{s}_{m-1}, \boldsymbol{y}_{m-1}) from memory if m > 0.
18:
                for i = m, m + 1, ..., k - 1 do
                                                                                                                                                                            \triangleright Transport \{s_i\} and \{y_i\} from \mathcal{T}_{u_k} to \mathcal{T}_{u_{k+1}}.
19:
                       \boldsymbol{s}_i \leftarrow T_k \boldsymbol{s}_i, \ \boldsymbol{y}_i \leftarrow T_k \boldsymbol{y}_i
20:
                end for
21:
                k \leftarrow k + 1
22:
23: end while
```

FIG. 6. Riemannian version of the L-BFGS algorithm to minimize (T)MERA energies, adapted from Ref. [84]. The optimization is started at a point $u_0 \in \mathcal{M}$ and stopped when the gradient norm falls below ε . For the approximation \tilde{H}_k of the inverse Hessian, ℓ vector pairs (s_i, y_i) with $i = k - \ell, \ldots, k - 1$ are kept in memory. The constants c_1 and c_2 enter the Wolfe conditions.

an inexact line search, and one chooses the next point $\boldsymbol{u}_{k+1} = \boldsymbol{r}_{\boldsymbol{u}_k,\boldsymbol{p}_k}(\tau_k)$ on the corresponding line (retraction curve) with $\tau_k \in \mathbb{R}$ such that the Wolfe conditions are obeyed. The latter require that both the function value and the gradient norm decrease sufficiently, where, in the Riemannian version, one rather considers the energy derivatives in the search direction. The BFGS algorithm [62, 84] modifies this procedure, avoiding the costly evaluation of the Hessian. Instead, one updates a positive definite approximation $H_k \in \text{End}(\mathcal{T}_{u_k})$ of the inverse Hessian. H_{k+1} is determined by requiring that the gradient of the new quadratic model at u_{k+1} , evaluated at u_k , should agree with the actual g_k . This is equivalent to the secant equation $s_k = H_{k+1}y_k$ with $s_k := T_k\tau_k p_k$ and the gradient change $\mathbf{y}_k := \mathbf{g}_{k+1} - T_k \mathbf{g}_k$, which are both elements of the tangent space $\mathcal{T}_{\mathbf{u}_{k+1}}$ as $T_k := T_{\mathbf{u}_k, \mathbf{p}_k}(\tau_k)$ denotes the vector transport. From the solution space of the secant equation, one chooses the matrix \tilde{H}_{k+1} that is closest to H_k in a suitable metric. Specifically, the BFGS update reads

$$\tilde{H}_{k+1} = V_k \tilde{H}_k V_k^{\dagger} + \rho_k s_k s_k^{\dagger} \tag{C12}$$

with $V_k := (\mathbb{1} - \rho_k \mathbf{s}_k \mathbf{y}_k^{\dagger}) T_k$ and $\rho_k := 1/(\mathbf{y}_k, \mathbf{s}_k)$. Finally, the L-BFGS algorithm [62, 84] avoids the increasing cost of operating with \tilde{H}_k by keeping the ℓ most recent triples $(\rho_k, \mathbf{s}_k, \mathbf{y}_k)$ in memory and computing an approximation of the inverse Hessian from them in each iteration.

The Riemannian L-BFGS algorithm that we employ, adapted from Ref. [84], is shown in Fig. 6. Note that, for numerical stability, after every retraction (C9), it may be

necessary to project the resulting point onto the manifold in order to avoid the accumulation of small numerical errors. For example, this can be done by a singular value decomposition for every Trotter gate and setting all singular values to one. If this is done, the finite numerical precision for the vector transport (C10) should have negligible effects, i.e., need not be corrected.

Appendix D: Different Trotter-gate parametrizations and XX-TMERA

The CNOT and CAN parametrizations for the Trotter gates of the TMERA are equivalent to the parametrization-free representation as U(4) unitaries, and, up to an irrelevant phase factor, one can transform between the parametrizations as described in Refs. [61, 71]. This equivalence is tested and confirmed by optimizing TMERA for the 1D transverse-field Ising model while scanning forth and back on the parameter interval $g \in [0.75, 1.25]$. Starting at g = 1.25, the optimization was initialized by a product state with $|\phi\rangle$ = $\hat{R}_{\hat{\sigma}^z}(\frac{\pi}{4})\hat{R}_{\hat{\sigma}^y}(\frac{\pi}{4})\hat{R}_{\hat{\sigma}^z}(\frac{\pi}{4})|0\rangle$ on every site. Figure 7 shows the accuracies of the energy densities e during the scanning procedure for TMERA in the CNOT and CAN parametrizations as well as the parametrization-free form ("Riemannian"). The results are compared to the corresponding fMERA optimization. The Euclidean L-BFGS algorithm [62, 63] was employed for the TMERA in the CAN and CNOT parametrizations and the Riemannian L-BFGS algorithm, as discussed in Appx. C.2,

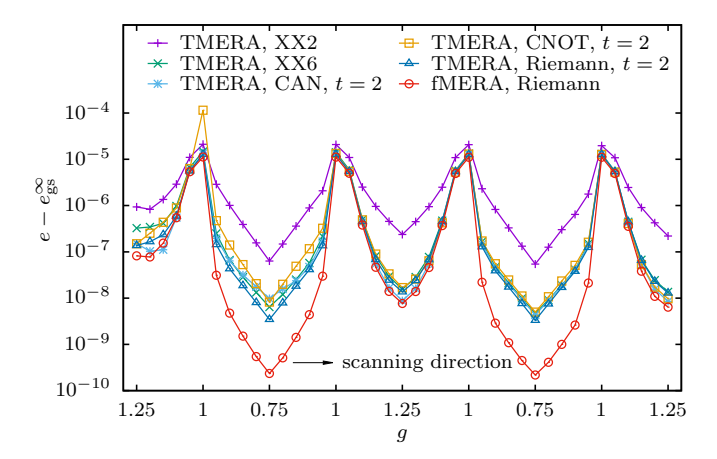


FIG. 7. Optimization and scanning with different parametrizations. Starting from a product state at g=1.25, we scan forth and back on the interval $0.75 \le g \le 1.25$, minimizing the MERA energy density e for the 1D transverse-field Ising model with the L-BFGS algorithm. This is done for homogeneous modified binary MERA with T=6 layers and bond dimension $\chi=2^q=8$. The TMERA tensors consist of t=2 Trotter steps, and XX-TMERA are simulated once with 2 and once with 6 XX Trotter steps per tensors.

was employed for the parametrization-free TMERA and fMERA. In all cases, the L-BFGS parameters were chosen as $\varepsilon = 10^{-12}$, $\ell = 9$, and $c_1 = 0.1$. We chose not to enforce the second Wolfe condition (line 14 in Fig. 6).

Although different TMERA parametrizations show differing energies in the early stages of the scanning procedure, they quickly converge. Without scanning, the parametrization-free TMERA is somewhat favorable. The explicit parametrizations in terms of rotation angles are more prone to getting stuck in local minima, whereas the local minima and saddle points for the parametrization-free form are entirely due to the structure of the TMERA manifold and the Hamiltonian. For random initial states, the parametrization-free form shows better convergence than the CNOT and CAN forms. As a simple example, note that the product state $|0\rangle^{\otimes N}$ is a stationary point for the CAN parametrization. The data in Fig. 2 was obtained by Riemannian optimization.

For the 1D TMERA, we chose the Trotter circuit of each tensor to consist of steps with U(4) gates on all odd qubit bonds and all even qubit bonds, alternatingly, as shown in Fig. 1c and in the left panel of Fig. 8. The

goal of this choice is to admit the generation of entanglement between any pair of qubits in a few Trotter steps. However, in the CNOT and CAN parametrizations, each Trotter gate features three elementary two-qubit gates; CNOT and $\hat{\sigma}^{\alpha} \otimes \hat{\sigma}^{\alpha}$ Ising rotations with $\alpha = x, y, z$, respectively. We have explored a different Trotterization approach, where layers of generic single-qubit gates alternate with XX Ising rotations. One XX Trotter step contains two layers of XX Ising rotations on odd and even bonds, respectively. For the same computational cost, characterized by the total number of two-qubit Ising rotations, causal cones in the XX Trotterization of the MERA tensors grow substantially faster than in the U(4)Trotterization. However, the benchmark simulations in Fig. 7 show no enhanced approximation accuracy. The energies for six XX Trotter steps per MERA tensor converge to approximately the same values as the energies for two U(4) Trotter steps per tensor. Improvements along these lines are a topic for future work.

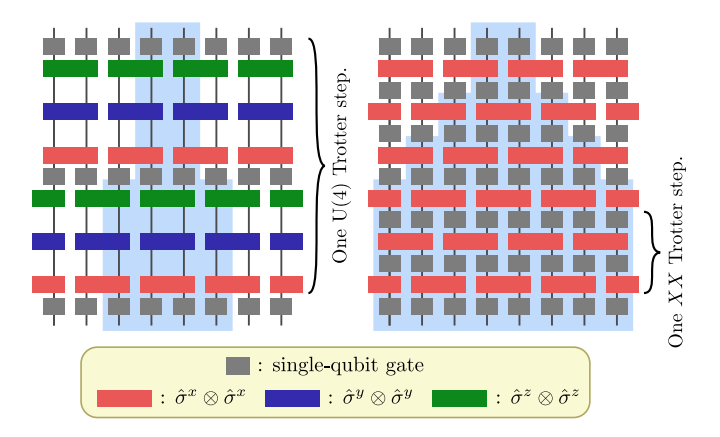


FIG. 8. XX-Trotterization. Left: In the TMERA considered so far, tensors are Trotterized into regular circuits of general 2-qubit Trotter gates \in U(4). For 1D systems, one Trotter step consists of such gates applied on all odd bonds and then on all even bonds. In the CAN form, each U(4) Trotter gate is realized by a sequence of two 1-qubit gates, followed by three Ising rotations generated by $\hat{\sigma}^{\alpha} \otimes \hat{\sigma}^{\alpha}$, and two 1-qubit gates. In every Trotter step, causal cones widen by at most three sites. Right: In the XX-TMERA, layers of 1-qubit gates alternate with layers of $\hat{\sigma}^{x} \otimes \hat{\sigma}^{x}$ Ising gates on even and odd bonds, respectively. One XX Trotter step contains two layers of Ising gates. In terms of the number of Ising gates, one U(4) Trotter step corresponds to three XX Trotter steps. For the latter, causal cones grow correspondingly faster.

W. M. C. Foulkes, L. Mitas, R. J. Needs, and G. Rajagopal, Quantum Monte Carlo simulations of solids, Rev. Mod. Phys. 73, 33 (2001).

^[2] M. Suzuki, S. Miyashita, and A. Kuroda, Monte Carlo Simulation of Quantum Spin Systems. I, Prog. Theor. Phys. 58, 1377 (1977).

^[3] O. F. Syljuåsen and A. W. Sandvik, Quantum Monte Carlo with directed loops, Phys. Rev. E 66, 046701 (2002).

^[4] N. V. Prokof'ev and B. V. Svistunov, Polaron Problem by Diagrammatic Quantum Monte Carlo, Phys. Rev. Lett. 81, 2514 (1998).

- [5] R. J. Baxter, Dimers on a rectangular lattice, J. Math. Phys. 9, 650 (1968).
- [6] S. R. White, Density matrix formulation for quantum renormalization groups, Phys. Rev. Lett. 69, 2863 (1992).
- [7] H. Niggemann, A. Klümper, and J. Zittartz, Quantum phase transition in spin-3/2 systems on the hexagonal lattice - optimum ground state approach, Z. Phys. B 104, 103 (1997).
- [8] F. Verstraete and J. I. Cirac, Renormalization algorithms for quantum-many body systems in two and higher dimensions, arXiv:cond-mat/0407066 (2004).
- [9] G. Vidal, Entanglement renormalization, Phys. Rev. Lett. 99, 220405 (2007).
- [10] U. Schollwöck, The density-matrix renormalization group in the age of matrix product states, Ann. Phys. 326, 96 (2011).
- [11] R. Orús, A practical introduction to tensor networks: Matrix product states and projected entangled pair states, Ann. Phys. 349, 117 (2014).
- [12] T. Barthel, C. Pineda, and J. Eisert, Contraction of fermionic operator circuits and the simulation of strongly correlated fermions, Phys. Rev. A 80, 042333 (2009).
- [13] P. Corboz and G. Vidal, Fermionic multiscale entanglement renormalization ansatz, Phys. Rev. B 80, 165129 (2009).
- [14] C. Pineda, T. Barthel, and J. Eisert, Unitary circuits for strongly correlated fermions, Phys. Rev. A 81, 050303(R) (2010).
- [15] C. V. Kraus, N. Schuch, F. Verstraete, and J. I. Cirac, Fermionic projected entangled pair states, Phys. Rev. A 81, 052338 (2010).
- [16] P. Corboz, G. Evenbly, F. Verstraete, and G. Vidal, Simulation of interacting fermions with entanglement renormalization, Phys. Rev. A 81, 010303(R) (2010).
- [17] E. Y. Loh, J. E. Gubernatis, R. T. Scalettar, S. R. White, D. J. Scalapino, and R. L. Sugar, Sign problem in the numerical simulation of many-electron systems, Phys. Rev. B 41, 9301 (1990).
- [18] M. Troyer and U.-J. Wiese, Computational complexity and fundamental limitations to fermionic quantum Monte Carlo simulations, Phys. Rev. Lett. 94, 170201 (2005).
- [19] L. Balents, Spin liquids in frustrated magnets, Nature 464, 199 (2010).
- [20] Y. Zhou, K. Kanoda, and T.-K. Ng, Quantum spin liquid states, Rev. Mod. Phys. 89, 025003 (2017).
- [21] Y. Shimizu, K. Miyagawa, K. Kanoda, M. Maesato, and G. Saito, Spin liquid state in an organic Mott insulator with a triangular lattice, Phys. Rev. Lett. 91, 107001 (2003).
- [22] F. L. Pratt, P. J. Baker, S. J. Blundell, T. Lancaster, S. Ohira-Kawamura, C. Baines, Y. Shimizu, K. Kanoda, I. Watanabe, and G. Saito, Magnetic and non-magnetic phases of a quantum spin liquid, Nature 471, 612 (2011).
- [23] A. Banerjee, C. A. Bridges, J.-Q. Yan, A. A. Aczel, L. Li, M. B. Stone, G. E. Granroth, M. D. Lumsden, Y. Yiu, J. Knolle, S. Bhattacharjee, D. L. Kovrizhin, R. Moessner, D. A. Tennant, D. G. Mandrus, and S. E. Nagler, Proximate Kitaev quantum spin liquid behaviour in a honeycomb magnet, Nature Materials 15, 733 (2016), article.
- [24] H. L. Stormer, D. C. Tsui, and A. C. Gossard, The fractional quantum Hall effect, Rev. Mod. Phys. 71, S298 (1999).

- [25] R. de Picciotto, M. Reznikov, M. Heiblum, V. Umansky, G. Bunin, and D. Mahalu, *Direct observation of a fractional charge*, Nature 389, 162 (1997).
- [26] J. G. Bednorz and K. A. Müller, Possible high-T_c superconductivity in the Ba-La-Cu-O system, Z. Phys. B 64, 189 (1986).
- [27] A. J. Leggett, What DO we know about high T_c?, Nat. Phys. 2, 134 (2006).
- [28] M. Fannes, B. Nachtergaele, and R. F. Werner, Finitely correlated states on quantum spin chains, Comm. Math. Phys. 144, 443 (1992).
- [29] S. Rommer and S. Östlund, A class of ansatz wave functions for 1D spin systems and their relation to DMRG, Phys. Rev. B 55, 2164 (1997).
- [30] T. Nishino, K. Okunishi, Y. Hieida, N. Maeshima, and Y. Akutsu, Self-consistent tensor product variational approximation for 3D classical models, Nucl. Phys. B 575, 504 (2000).
- [31] M. A. Martín-Delgado, M. Roncaglia, and G. Sierra, Stripe ansätze from exactly solved models, Phys. Rev. B 64, 075117 (2001).
- [32] F. Verstraete, M. M. Wolf, D. Perez-Garcia, and J. I. Cirac, Criticality, the area law, and the computational power of projected entangled pair states, Phys. Rev. Lett. 96, 220601 (2006).
- [33] G. Vidal, Class of quantum many-body states that can be efficiently simulated, Phys. Rev. Lett. 101, 110501 (2008).
- [34] G. Evenbly and G. Vidal, Quantum criticality with the multi-scale entanglement renormalization ansatz, arXiv:1109.5334 (2013).
- [35] J. Jordan, R. Orús, G. Vidal, F. Verstraete, and J. I. Cirac, Classical simulation of infinite-size quantum lattice systems in two spatial dimensions, Phys. Rev. Lett. 101, 250602 (2008).
- [36] R. Orús and G. Vidal, Simulation of two-dimensional quantum systems on an infinite lattice revisited: Corner transfer matrix for tensor contraction, Phys. Rev. B 80, 094403 (2009).
- [37] L. Cincio, J. Dziarmaga, and M. M. Rams, Multiscale entanglement renormalization ansatz in two dimensions: quantum Ising model, Phys. Rev. Lett. 100, 240603 (2008).
- [38] G. Evenbly and G. Vidal, Entanglement renormalization in two spatial dimensions, Phys. Rev. Lett. 102, 180406 (2009).
- [39] J. R. McClean, J. Romero, R. Babbush, and A. Aspuru-Guzik, The theory of variational hybrid quantum-classical algorithms, New J. Phys. 18, 023023 (2016).
- [40] T. Barthel, J. Lu, and G. Friesecke, On the closedness and geometry of tensor network state sets, arXiv:2108.00031 (2021).
- [41] F. Barratt, J. Dborin, M. Bal, V. Stojevic, F. Pollmann, and A. G. Green, Parallel quantum simulation of large systems on small NISQ computers, npj Quantum Inf. 7, (2021).
- [42] J.-G. Liu, Y.-H. Zhang, Y. Wan, and L. Wang, Variational quantum eigensolver with fewer qubits, Phys. Rev. Research 1, 023025 (2019).
- [43] A. Smith, B. Jobst, A. G. Green, and F. Pollmann, Crossing a topological phase transition with a quantum computer, arXiv:1910.05351 (2019).
- [44] M. Foss-Feig, D. Hayes, J. M. Dreiling, C. Figgatt, J. P. Gaebler, S. A. Moses, J. M. Pino, and A. C. Potter,

- Holographic quantum algorithms for simulating correlated spin systems, Phys. Rev. Research 3, 033002 (2021).
- [45] R. J. Schoelkopf and S. M. Girvin, Wiring up quantum systems, Nature 451, 664 (2008).
- [46] M. H. Devoret and R. J. Schoelkopf, Superconducting circuits for quantum information: An outlook, Science 339, 1169 (2013).
- [47] J. I. Cirac and P. Zoller, Quantum computations with cold trapped ions, Phys. Rev. Lett. 74, 4091 (1995).
- [48] R. Blatt and D. Wineland, Entangled states of trapped atomic ions, Nature 453, 1008 (2008).
- [49] M. Rowe, A. Ben-Kish, B. DeMarco, D. Leibfried, V. Meyer, J. Beall, J. Britton, J. Hughes, W. Itano, B. Jelenkovic, C. Langer, T. Rosenband, and D. Wineland, Transport of quantum states and separation of ions in a dual rf ion trap, Quantum Info. Comput. (2002).
- [50] W. K. Hensinger, S. Olmschenk, D. Stick, D. Hucul, M. Yeo, M. Acton, L. Deslauriers, C. Monroe, and J. Rabchuk, T-junction ion trap array for two-dimensional ion shuttling, storage, and manipulation, Appl. Phys. Lett. 88, 034101 (2006).
- [51] A. Walther, F. Ziesel, T. Ruster, S. T. Dawkins, K. Ott, M. Hettrich, K. Singer, F. Schmidt-Kaler, and U. Poschinger, Controlling fast transport of cold trapped ions, Phys. Rev. Lett. 109, 080501 (2012).
- [52] L. Kadanoff, Scaling laws for Ising models near Tc, Physics 2, 263 (1966).
- [53] R. Jullien, J. Fields, and S. Doniach, Kondo lattice: Realspace renormalization-group approach, Phys. Rev. Lett. 38, 1500 (1977).
- [54] S. D. Drell, M. Weinstein, and S. Yankielowicz, Quantum field theories on a lattice: Variational methods for arbitrary coupling strengths and the Ising model in a transverse magnetic field, Phys. Rev. D 16, 1769 (1977).
- [55] A. Barenco, C. H. Bennett, R. Cleve, D. P. DiVincenzo, N. Margolus, P. Shor, T. Sleator, J. A. Smolin, and H. Weinfurter, *Elementary gates for quantum computation*, Phys. Rev. A **52**, 3457 (1995).
- [56] M. Möttönen, J. J. Vartiainen, V. Bergholm, and M. M. Salomaa, Quantum circuits for general multiqubit gates, Phys. Rev. Lett. 93, 130502 (2004).
- [57] V. V. Shende, S. S. Bullock, and I. L. Markov, Synthesis of quantum-logic circuits, IEEE Trans. Comput.-Aided Des. Integr. Circuits Syst. 25, 1000 (2006).
- [58] R. Iten, R. Colbeck, I. Kukuljan, J. Home, and M. Christandl, Quantum circuits for isometries, Phys. Rev. A 93, 032318 (2016).
- [59] G. Evenbly and G. Vidal, Algorithms for entanglement renormalization, Phys. Rev. B 79, 144108 (2009).
- [60] F. Vatan and C. Williams, Optimal quantum circuits for general two-qubit gates, Phys. Rev. A 69, 032315 (2004).
- [61] V. V. Shende, I. L. Markov, and S. S. Bullock, Minimal universal two-qubit controlled-NOT-based circuits, Phys. Rev. A 69, 062321 (2004).
- [62] J. Nocedal and S. J. Wright, Numerical Optimization, 2nd ed. (Springer, New York, 2006).
- [63] D. C. Liu and J. Nocedal, On the limited memory BFGS method for large scale optimization, Math. Program. 45, 503 (1989).
- [64] C. D. Bruzewicz, J. Chiaverini, R. McConnell, and J. M. Sage, Trapped-ion quantum computing: Progress and challenges, Appl. Phys. Rev. 6, 021314 (2019).
- [65] S. Sheldon, L. S. Bishop, E. Magesan, S. Filipp, J. M. Chow, and J. M. Gambetta, Characterizing errors on

- qubit operations via iterative randomized benchmarking, Phys. Rev. A **93**, 012301 (2016).
- [66] D. C. McKay, S. Sheldon, J. A. Smolin, J. M. Chow, and J. M. Gambetta, *Three-qubit randomized benchmarking*, Phys. Rev. Lett. **122**, 200502 (2019).
- [67] M. Kjaergaard, M. E. Schwartz, J. Braumüller, P. Krantz, J. I.-J. Wang, S. Gustavsson, and W. D. Oliver, Superconducting qubits: Current state of play, Annu. Rev. Condens. Matter Phys. 11, 369 (2020).
- [68] A. Sørensen and K. Mølmer, Quantum computation with ions in thermal motion, Phys. Rev. Lett. 82, 1971 (1999).
- [69] S. Debnath, N. M. Linke, C. Figgatt, K. A. Landsman, K. Wright, and C. Monroe, Demonstration of a small programmable quantum computer with atomic qubits, Nature 536, 63 (2016).
- [70] D. Maslov, Basic circuit compilation techniques for an ion-trap quantum machine, New J. Phys. 19, 023035 (2017).
- [71] B. Kraus and J. I. Cirac, Optimal creation of entanglement using a two-qubit gate, Phys. Rev. A 63, 062309 (2001).
- [72] J. Zhang, J. Vala, S. Sastry, and K. B. Whaley, Geometric theory of nonlocal two-qubit operations, Phys. Rev. A 67, 042313 (2003).
- [73] W. F. Stinespring, Positive functions on C*-algebras, Proc. Am. Math. Soc. 6, 211 (1955).
- [74] M. A. Nielsen and I. L. Chuang, Quantum Computation and Quantum Information (Cambridge University Press, Cambridge, 2000).
- [75] Y.-Y. Shi, L.-M. Duan, and G. Vidal, Classical simulation of quantum many-body systems with a tree tensor network, Phys. Rev. A 74, 022320 (2006).
- [76] V. Murg, F. Verstraete, O. Legeza, and R. M. Noack, Simulating strongly correlated quantum systems with tree tensor networks, Phys. Rev. B 82, 205105 (2010).
- [77] I. H. Kim and B. Swingle, Robust entanglement renormalization on a noisy quantum computer, arXiv:1711.07500 (2017).
- [78] K. Wright, K. M. Beck, S. Debnath, and al., Benchmarking an 11-qubit quantum computer, Nat. Commun. 10, (2019).
- [79] N. M. Linke, D. Maslov, M. Roetteler, S. Debnath, C. Figgatt, K. A. Landsman, K. Wright, and C. Monroe, Experimental comparison of two quantum computing architectures, Proc. Natl. Acad. Sci. U.S.A. 114, 3305 (2017).
- [80] K. Mølmer and A. Sørensen, Multiparticle entanglement of hot trapped ions, Phys. Rev. Lett. 82, 1835 (1999).
- [81] A. Sørensen and K. Mølmer, Entanglement and quantum computation with ions in thermal motion, Phys. Rev. A 62, 022311 (2000).
- [82] J. Li, X. Yang, X. Peng, and C.-P. Sun, Hybrid quantumclassical approach to quantum optimal control, Phys. Rev. Lett. 118, 150503 (2017).
- [83] G. G. Guerreschi and M. Smelyanskiy, Practical optimization for hybrid quantum-classical algorithms, arXiv:1701.01450 (2017).
- [84] W. Huang, K. A. Gallivan, and P.-A. Absil, A Broyden class of quasi-Newton methods for Riemannian optimization, SIAM Journal on Optimization 25, 1660 (2015).
- [85] S. T. Smith, in Hamiltonian and Gradient Flows, Algorithms, and Control, Vol. 3 of Fields Institute Communications (AMS, USA, 1994), Chap. Optimization techniques on Riemannian manifolds, p. 113.
- [86] M. Hauru, M. Van Damme, and J. Haegeman, Rieman-

- $nian\ optimization\ of\ isometric\ tensor\ networks,$ SciPost Phys. ${\bf 10},\ (2021).$
- [87] I. A. Luchnikov, M. E. Krechetov, and S. N. Filippov, Riemannian geometry and automatic differentiation for

optimization problems of quantum physics and quantum technologies, New J. Phys. ${f 23},\,073006$ (2021).